Journal of Applied Physics

Photoluminescence spectrum of divacancy in porous and nanocrystalline cubic silicon carbide

Cite as: J. Appl. Phys. **131**, 071102 (2022); https://doi.org/10.1063/5.0080514
Submitted: 01 December 2021 • Accepted: 02 February 2022 • Published Online: 18 February 2022

András Csóré, Nain Mukesh, Gyula Károlyházy, et al.

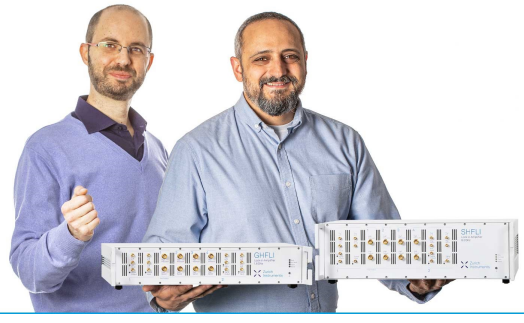

Journal of Applied Physics TUTORIAL scitation.org/journal/jap

Photoluminescence spectrum of divacancy in porous and nanocrystalline cubic silicon carbide

Cite as: J. Appl. Phys. **131**, 071102 (2022); doi: 10.1063/5.0080514
Submitted: 1 December 2021 · Accepted: 2 February 2022 ·
Published Online: 18 February 2022

András Csóré,[1] Nain Mukesh,[2] Gyula Károlyházy,[2] David Beke,[1,2] and Adam Gali[1,2,a)]

AFFILIATIONS

[1]Department of Atomic Physics, Institute of Physics, Budapest University of Technology and Economics, Műegyetem rakpart 3., H-1111 Budapest, Hungary
[2]Wigner Research Centre for Physics, PO. Box 49, Budapest H-1525, Hungary

Note: This paper is part of the Special Topic on Defects in Semiconductors.
[a)]**Author to whom correspondence should be addressed:** gali.adam@wigner.hu

ABSTRACT

The divacancy in silicon carbide (SiC) is a prominent solid state defect quantum bit that bears a relatively strong fluorescence and optically detected magnetic resonance contrast (ODMR) at room temperature. These properties exemplify it for quantum sensing of biological molecules. To this end, we previously developed a top-down method to create divacancies in cubic SiC nanoparticles (NPs) as non-perturbative ODMR biomarkers. In this process, large SiC particles are synthesized and then stain etched to form porous SiC and then ultrasonication and filtering are applied to the solution to extract few nanometer diameter SiC NPs. We called this process no-photon exciton generation chemistry (NPEGEC). We showed that by adding aluminum to carbon and silicon in the synthesis process of cubic SiC, one can engineer divacancy defects in SiC NPs by NPEGEC. An alternative traditional way to introduce vacancies to the SiC lattice is irradiation. Here, we compare the fluorescence spectra of divacancies as created by neutron irradiation in porous cubic SiC and NPEGEC technique in SiC NPs, and the results are analyzed in detail by means of first principles calculations. We find that the irradiation technique produces a larger shift in the fluorescence spectrum with residual background fluorescence than that for divacancies in SiC NPs, which is most likely caused by the parasitic defects left after irradiation and annealing in the former sample. These results imply that the chemistry technique applied to prepare divacancies in few nanometer SiC NPs may preserve the bulk-like quality of divacancy quantum bits near the surface.

I. INTRODUCTION

Solid state point defects exhibiting paramagnetic electronic ground and an optical excited state are forefront contenders as building blocks of certain quantum technology devices.[1,2] In particular, defects in silicon carbide (SiC) are applicable as single-photon emitters being pivotal in quantum information processing,[3–7] ultrasensitive nanosensors in magnetometry[8–13] or thermometry,[9,14] and quantum bits (qubits).[15,16] The divacancy (V_CV_{Si}) in SiC—consisting of a silicon vacancy (V_{Si}) and a neighboring carbon vacancy (V_C)—is an outstanding member of the wide palette of SiC defects. V_CV_{Si} in SiC exhibits several desirable properties, making it a promising qubit candidate. In particular, its electronic structure introduces spin triplet ($S = 1$) ground and optically excited states.[15,17–21]

The corresponding optical transitions, i.e., the zero-phonon lines (ZPLs), are around 1100 nm with relatively long-tail phonon sideband up to 1400 nm falling into the near-infrared (NIR) region.[16,22–24] In particular, the majority of emission band fall into the so-called second biological window[25] where the absorption and autofluorescence of water and biological molecules are minimal. This property makes the divacancy color center in small SiC nanocrystal desirable candidate as an ultrasensitive biomarker.[26–28]

We focus our attention on the cubic SiC or 3C SiC matrix hosting the divacancy defect (see Fig. 1) because divacancy centers were prepared in such polytype of SiC in nanocrystalline form.[28] We note that the coherence times and fluorescence properties of divacancy quantum bits in 3C SiC are all favorable similar to their counterparts in other polytypes of SiC;[16] however, its optical properties are largely unexplored, in particular, in porous and nanocrystalline 3C SiC matrix. We note that the photoluminescence (PL) signal of the divacancy in bulk 3C SiC can be observed at room temperature.[29]

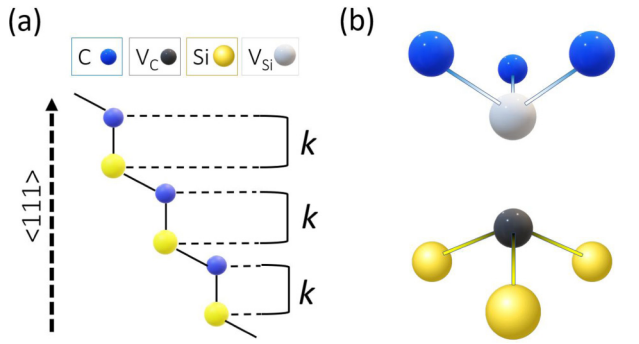

FIG. 1. (a) Lattice structure of the perfect 3C SiC. Crystal direction of ⟨111⟩ is indicated. (b) Microscopic structure of the divacancy defect. The color code of atoms is indicated. We note that the symmetry axis of divacancy is pointing along the ⟨111⟩ axis of the crystal.

In this brief report, we study the room temperature divacancy fluorescence spectrum from neutron-irradiated and annealed porous SiC (p-SiC) as well as from such few nanometer diameter SiC NPs (SiC-NP) that were created by chemistry without any invasive techniques toward the crystal structure. We apply Kohn–Sham spinpolarized density functional theory (DFT) calculations in 3C SiC to analyze the data. The theory starts with the temperature-dependent spectrum by comparing the results with the literature data in bulk 3C SiC at cryogenic temperatures. Our paper is organized as follows: we describe the preparation of divacancy defects in porous and nanocrystalline 3C SiC, the calculation method of the photoluminescence line shape, and the DFT simulation parameters in Sec. II. We report and discuss our results starting with the theoretical description and continuing with a comparison to the experimental data in Sec. III. Our conclusions are summarized in Sec. IV.

II. METHODOLOGY

A. Experimental setup

In our investigations, two types of cubic 3C SiC samples with divacancy defects were prepared: porous, neutron-irradiated, and annealed SiC samples labeled as p-SiC and SiC nanoparticles by etching the porous SiC together with using other chemistry treatments as explained below, which we label as SiC-NP.

Porous etching creates a nanostructured material from bulk SiC, while neutron-irradiation and subsequent annealing can create V_CV_{Si} defects. The used SiC source for porous etching and the applied chemistry was described in our previous article.[28] Briefly, Si (99%, 325 mesh, Sigma Aldrich) and C [Norit A supra, surface area (BET), 1700 m^2/g] in a 1:1 ratio and 3 wt. % PTFE (polytetrafluoroethylene) (1 μm particle size, Sigma Aldrich) and 5 wt. % Al powder (95%, <5 μm, Sigma Aldrich) were mixed in a ball mill for 12 h, placed into a graphite crucible, and annealed to about 1250 °C in an argon atmosphere for 8 min using an induction furnace (Stanelco STX25-DF1, 9.5 kV, 3.5 A, 288 kHz) to prepare SiC powder. The samples were then annealed at 650 °C in air for 10 h and etched with HNO_3:H_2O 1:1 and HF:HNO_3:H_2O 1:1:10 in order to remove unreacted carbon, Al, and Si. According to the XRD measurement, pure SiC powder has about 40 nm crystallite size, and 100–200 nm particle size. The synthesized SiC powder has a cubic polytype with hexagonal stacking faults. Al and PTFE concentration regulates the stacking fault concentration. These powders also contain V_{Si} and E centers formed during the synthesis (see Ref. 28 and references therein). Aluminum can react with SiC crystals, and the chemical reaction slowly removes Si and C atoms from the surface of SiC. The reaction is much faster with Si and C, and this etching reaction happens during the rapid crystal growth. As a result, the vacancies created by etching are buried in SiC crystals. To create nanostructured SiC with divacancies, SiC powder was etched using no-photon exciton generation chemistry (NPEGEC)[30] as follows. 5 g of SiC was etched in a 40 ml HF:HNO_3 3:1 mixture at 180 °C using a high-pressure acid digestion chamber (DAB-3, 250 ml, Berghoff GmbH). NPEGEC creates porous SiC. The porous SiC was either neutron-irradiated (10^{18} n/cm^2 0.18–2.5 MeV, TRIGA Mark II Reactor, TU Vienna) and annealed at 750 °C for 2 h to create divacancies in the nanostructure (p-SiC) or was sonicated in DI water for 3 h then annealed at 140 °C to create SiC-NP (see Fig. 2). To make sure that the SiC-NP sample contains only 4–6 nm particles, after ultrasonication, the suspension was centrifuged down (BioFuge Primo, ThermoFischer, 8000 rpm, 40 min) and the supernatant was filtered through a 0.1 μm syringe filter, a 20 nm syringe filter (Whatman® Anotop® 10, Sigma Aldrich), and a Pall Macrosep 100 kDa centrifuge filter. A Pall Macrosep, 10 kDa filter, was used to remove species smaller than 3 nm, and, finally, the retentate was used. The retentate was diluted with DI water and sonicated for 30 min. These nanoparticles contain E centers according to the photoluminescence (PL) and electron spin resonance (ESR) measurements.[28] Annealing of the nanoparticles at 140 °C for 2 h transforms some of these E centers into divacancies. The presence of the divacancies was proved by PL, ESR, and optically detected magnetic resonance (ODMR) measurements.[28] Here, only fluorescence spectra are presented by comparing the data from p-SiC samples.

Fluorescence spectra were recorded at room temperature with a Horiba Jobin-Yvon NanoLog FL3-2iHR spectrophotometer equipped with an iHR-320 grating spectrometer and a Symphony liquid-nitrogen cooled InGaAs CCD. A Roithner RLTMDL-785-1W-1 laser was used for 785-nm excitation. The applied power was 250 mW, and the spot size was about 15 mm. Samples were drop casted on a Si or a quartz substrate.

B. Huang–Rhys theory of the PL spectrum

The PL emission spectrum including phonon-assisted electronic transitions were obtained by applying the Huang–Rhys (HR)[31] theory as implemented by Gali *et al.*,[32] also inspired by a previous study (HR) theory.[33] The strength of the electron–phonon coupling is represented by the HR factor [$S(\hbar\omega)$]. A detailed derivation of S can be found in Refs. 32–34. The S factor has an intimate connection with the Debye–Waller (DW) factor (w),[35,36] which is the ratio of the ZPL intensity and the total intensity that can be directly read from the experimental spectrum (if there are no overlapping spectra in the critical wavelength region). The relation between the two is $w = \exp(-S)$.

We provide here the key equations to generate the fluorescence or photoluminescence (PL) line shape. The PL spectrum $[I^{EM}(\hbar\omega)]$ can be expressed as[33]

$$I^{EM}(\hbar\omega) = C^{EM}\omega^3\mu_{EG}^2 \sum_{n,m} c_m(T)\left|\left\langle \Theta_{ES}^m(Q)\middle|\Theta_{GS}^n(Q)\right\rangle\right|^2 \delta(E_{ES}^m - E_{GS}^n - \hbar\omega), \quad (1)$$

where the transitions from the corresponding vibronic substates of the excited state (ES), indexed by m, to those of the ground state (GS) with the index n are also considered establishing the phonon sideband (PSB) besides the ZPL. If $m = n = 0$, $I^{EM}(\hbar\omega)$ yields the intensity of ZPL. In Eq. (1), $\boldsymbol{\mu}_{EG}$ is the corresponding matrix element (which is now a three component vector with the length of μ_{EG}) of the transition dipole moment operator, $\hat{\boldsymbol{\mu}}_{EG} = q\sum_j \hat{\mathbf{r}}_j$ defined as

$$\boldsymbol{\mu}_{EG} = \langle \Psi_{ES}(\mathbf{r}_i)|\hat{\boldsymbol{\mu}}_{EG}|\Psi_{GS}(\mathbf{r}_i)\rangle \quad (2)$$

and $\hbar\omega$ is the photon energy. The prefactor ω^3 in Eq. (1) consists of the photon density of states (DOS) causing spontaneous emission ($\sim\omega^2$) and the perturbing field of those photons ($\sim\omega$). In contrast, the absorption spectrum is a linear function of ω since no spontaneous emission is involved. In Eq. (1), C^{EM} is a constant that depends on the materials and technicalities of the measurements. Since C^{EM} and $\hat{\boldsymbol{\mu}}_{EG}$ are constants across the spectrum, we used Eq. (3) as the PL line shape $[L^{EM}(\hbar\omega)]$ defined as

$$L^{EM}(\hbar\omega) = \omega^3 \sum_{n,m} c_m(T)\left|\left\langle \Theta_{GS}^n(Q)\middle|\Theta_{ES}^m(Q)\right\rangle\right|^2 \delta(E_{ES}^m - E_{GS}^n - \hbar\omega). \quad (3)$$

In Eqs. (1) and (3), the overlapping integral of the GS and ES vibrational states is denoted by $\Theta_{ES}^m(Q)$ and $\Theta_{GS}^n(Q)$, respectively. The partial HR factor of ω_k vibration is associated with the overlap integral where the sum of partial HR factors yields the total HR factor S. These can be calculated as given below.

In the HR framework, three basic assumptions are established as (i) normal modes, (ii) vibrational frequencies are identical in the initial and final states, and (iii) the equilibrium configuration is shifted by $\Delta\mathbf{Y}$ in the final state with respect to the initial nuclear configuration. Generalized nuclear configuration weighted by the nuclear masses ($\mathbf{Y}$) can be defined as $\mathbf{Y} = \mathbf{M}^{\frac{1}{2}}\mathbf{X}$, where $\mathbf{X} = (\mathbf{R}_1, \ldots, \mathbf{R}_N) = (X_1, Y_1, Z_1, \ldots, X_N, Y_N, Z_N)$ is a vector constructed by the nuclear coordinates and

$$\mathbf{M} = \begin{bmatrix} M_1 & & & & & \\ & M_1 & & & & \\ & & M_1 & & & \\ & & & M_2 & & \\ & & & & \ddots & \\ & & & & & M_N \end{bmatrix} \quad (4)$$

is the mass tensor. The partial HR factor (S_k) can be calculated as the scalar product of the normal vectors of mode k ($\mathbf{Y}_0^k$) and the displacement vector of $\Delta\mathbf{Y}$ as

$$S_k = (\Delta\mathbf{Y}^T\mathbf{Y}_0^k)^2. \quad (5)$$

By Eq. (5), the (total) HR factor (S) can be defined as

$$S = \sum_k^{3N-6} S_k. \quad (6)$$

While the partial HR factor indicates the weight of phonon mode k in the corresponding electronic transition, a total HR factor gives a measure for the strength of the overall electron–phonon coupling. Accordingly, in the case of $S = 0$, no phonon sideband appears in the PL spectrum, only the zero-phonon line (ZPL) representing the electronic transition with no phonon assistance. By using the HR factors overlapping integral of the initial and final vibrational wavefunctions describing the line shape of the spectrum can be written as

$$\left\langle \Theta_f^m(Q)\middle|\Theta_i^n(Q)\right\rangle = \prod_k \langle m_k|n_k\rangle, \quad (7)$$

where $\Theta_i^m(Q)$ and $\Theta_f^n(Q)$ stand for the vibrational wavefunctions of the initial and final states, respectively, m_k and n_k stand for the phonon occupation of mode k in the final and initial states with the corresponding n and m quantum numbers, respectively, and

$$|\langle m_k|n_k\rangle| = e^{-S_k}\frac{S_k^{m-n}}{(m-n)!}. \quad (8)$$

At $T = 0$ K, the lowest energy phonon state is occupied in the electronic excited state, i.e., $m = 0$. As the temperature raised higher energy m phonon states is occupied. The Boltzmann distribution function may be applied at a given temperature (T) for calculating the occupation of the ω_k phonon state, which is given by $c_m(T)$ in Eqs. (1) and (3). By defining $\boldsymbol{\varepsilon}$ as the vibronic excited state's (m) energy in the electronic excited state

$$\boldsymbol{\varepsilon}_m = E_{ES}^m - E_{ES}^0 \quad (9)$$

and $c_m(T)$ can be given as

$$c_m = \frac{\exp\left(\frac{-\boldsymbol{\varepsilon}_m}{k_BT}\right)}{\sum_m \exp\left(\frac{-\boldsymbol{\varepsilon}_m}{k_BT}\right)}. \quad (10)$$

By this way, the temperature dependent PL line shape may be obtained. We note that all HR spectra presented in this work are normalized.

The temperature dependent width of ZPL emission is not incorporated in this theory. Principally, the ZPL width is associated with the optical lifetime at $T = 0$ K for a single divacancy defect but may rapidly broaden at elevated temperatures for dynamic Jahn–Teller systems in the excited state. Indeed, the ^3E ES of divacancy is a dynamic Jahn–Teller state similar to the NV center in diamond, which leads to a T^5 dependence for broadening the ZPL

peak because of the Raman transition of acoustic phonons.[37] As no experimental data are available for the temperature dependent linewidth of the ZPL emission for divacancy in 3C SiC, we employ the theory from the NV center in diamond, but the prefactor before the T^5 dependence is estimated to be two orders of magnitude larger because SiC has much lower Debye-temperature than that of diamond. As a consequence, the broadening of ZPL line becomes 10 meV at room temperature. This could be a rough but plausible approximation as the two systems are very similar to each other but with stronger temperature dependence in SiC than that in diamond.[16,20,21]

C. Computational methodology

In order to obtain the temperature dependent PL spectrum, we calculated the ground and optical excited states by means of HSE06 range-separated hybrid functional[38] accompanied by the ΔSCF method[39] in excited state calculations. The divacancy defect was modeled in a 512-atom 3C SiC supercell. Fully relaxed geometries were obtained by minimizing the interatomic forces between using the threshold of 0.01 eV/Å. Kohn–Sham wavefunctions were expanded in the plane wave basis set with the cutoff energy of 420 eV. In the calculations, only valence electrons were treated explicitly, core-electrons were considered in the framework of projector augmented wave (PAW) method[40] as implemented in the Vienna *Ab initio* Simulation Package (VASP).[41]

In the excited state electronic structure, a strong electron–phonon coupling may emerge (see Sec. III A), which can be described as the Jahn–Teller (JT) effect.[42] Accordingly, the symmetry will be reduced from C_{3v} to C_{1h} by coupling with phonons in order to split the corresponding e level, lifting the degeneracy in total energy. In the calculation of the emission spectrum, we use static JT distorted geometries, exhibiting the lowest total energy. For the vibrational modes, we calculated the dynamical matrix in the ground state containing the second order derivatives of the total energy by means of the Perdew–Burke–Ernzerhof (PBE)[43] functional.

For the analysis of the phonon sideband, we applied the inverse participation ratio (IPR) for quantifying the localization of quasilocal phonon modes[33,44] defined as

$$\mathrm{IPR}_k = \frac{N\sum_i \mathbf{u}_i^4}{(\sum \mathbf{u}_i^2)^2}, \tag{11}$$

where $\mathbf{u}_i$ is the vector displacement amplitude of the ith atom in the kth phonon mode and N is the number of atoms in the supercell, that is, $N = 512$ in our case. Consequently, the IPR falls in the region of $[1, N]$. When all atoms participating in a phonon mode possess equal amplitudes in their motion, the IPR is equal to the number of atoms vibrating in a certain phonon mode.

III. RESULTS AND DISCUSSION

The PL line shape of divacancy in 3C SiC depends on the intricate details of the electronic structure of the defect in the ground state and the excited state electronic configurations as well as the change in the geometry upon illumination. Materials imperfections such as strain caused by either the presence of other nearby point defects or the surface for shallow lying divacancy defects may shift and broaden the PL spectrum, which cause inhomogeneous broadening in the PL spectrum recorded for the ensemble of divacancy defects. In high quality chemical vapor deposited (CVD) 3C SiC layers, the strain is present less, although, typically, 3C SiC is grown on top of the silicon substrate and the lattice mismatch between the substrate and 3C SiC layers may affect the PL spectrum of divacancy at a deeper region in the host crystal far from the interface.

In first principles simulations, one can study the intrinsic nature of the emission of an isolated defect. However, the concentration of divacancy defect in a 512-atom supercell is still much higher than that in experiments but the strain field generated by the defect decays at the Wigner–Seitz boundaries of the 512-atom supercell; thus, it may be taken as nearly isolated in a perfect 3C SiC environment. Therefore, we apply the strategy that we first analyze the electronic structure and PL line shape from first principles (Sec. III A) and compare the results to the highest quality PL spectrum of divacancy in CVD-grown 3C SiC layers at low temperature from Ref. 16 (Sec. III B), which is a reference PL spectrum of divacancy in 3C SiC. Here, we extend the simulation toward elevated temperatures critical for biomarker applications. Finally, we report our experimental PL spectra on neutron irradiated porous 3C SiC and nanocrystalline 3C SiC NPs at room temperature by analyzing the change in the spectrum with respect to the reference PL spectrum and its implication on the preparation of quantum sensors (Sec. III C).

A. Electronic structure

The divacancy defect introduces an a_1 and a degenerate e level to the bandgap (2.29 eV) as depicted in Fig. 3. In the ground state, the lower-in-energy non-degenerate a_1 level is fully occupied by two electrons, while the double degenerate e level is occupied by two electrons with parallel spins, establishing the $^3A_2$ spin triplet state. The optical excited state is formed by promoting an electron in the minority spin channel from the a_1 level to the degenerate e level, yielding the $a_1(1)e(3)$ electronic configuration providing the many-body wavefunction of ^3E. However, the fractional occupation of the e level may give rise to electron–phonon coupling described by the JT effect. In this way, the symmetry described by the C_{3v} point group will be reduced to C_{1h} symmetry lifting the degeneracy of the e level resulting in non-degenerate levels of a' and a''. The PL spectrum is calculated in the distorted geometry in the electronic excited state, which then includes the contribution of e phonons in the phonon sideband.[45]

B. Simulated temperature-dependent PL spectrum

In this section, we report the PL spectrum of the divacancy defect in 3C SiC. First, we discuss the $T = 0$ K case depicted in Fig. 4 as obtained from DFT calculations. We note that we do not include here any inhomogeneous broadening, thus the simulated spectrum refers to the ideal case when all the defects are well isolated in a perfect 3C SiC environment. The calculated ZPL is located at 1.14 eV (1087.6 nm), while the corresponding experimental value is at 1.12 eV (1107.0 nm)[16] demonstrating the

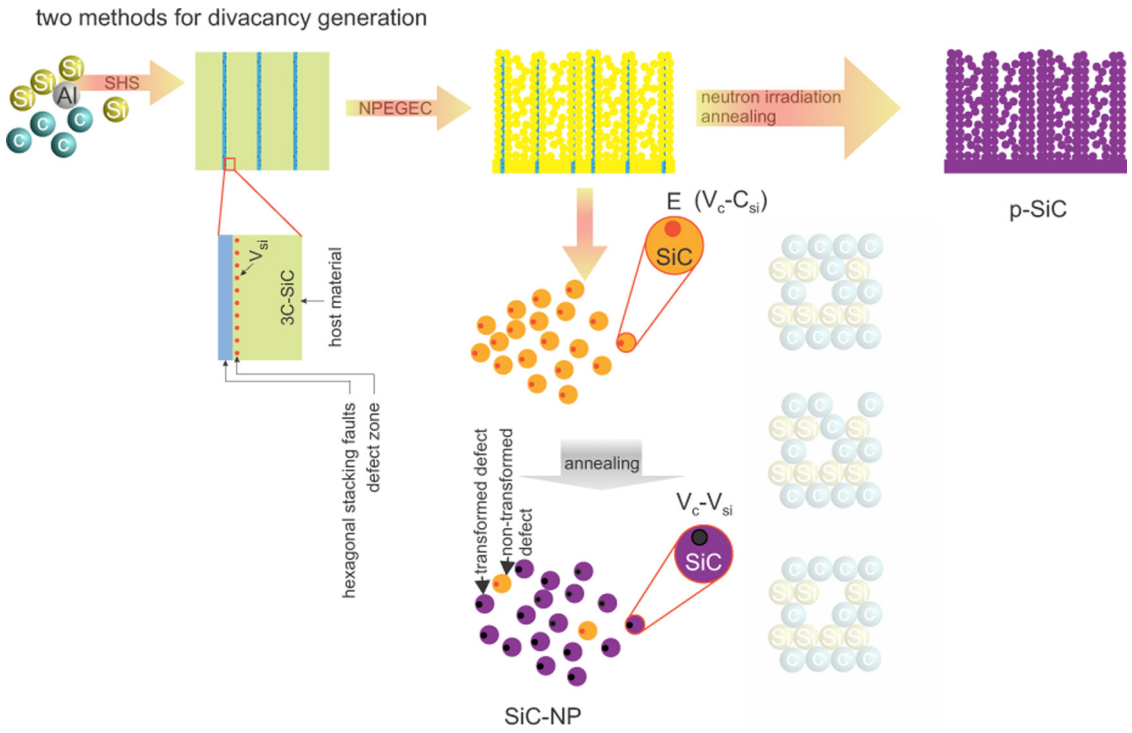

FIG. 2. Schematic diagram about the preparation of the cubic 3C SiC samples with divacancies.

accuracy of the HSE06 functional in these calculations. We note that ZPL energy in 3C SiC is close to those of $V_C V_{Si}$ configurations in 4H SiC, varying from 1.10 eV to 1.15 eV.[46,29] In Fig. 4, the simulated ZPL energy is aligned to the experimental value for the sake of direct comparison of the simulated and observed phonon sideband. The calculated HR factor $S = 2.71$ yields a DW factor of $w = 0.07$ which is a higher value than that for the divacancy defects in 4H SiC.[34] Indeed, low-temperature PL experiments confirm these results as $w = 0.073 \pm 0.003$ have been observed for divacancy in 3C SiC and lower w values were detected for divacancy configurations in 4H SiC.[16]

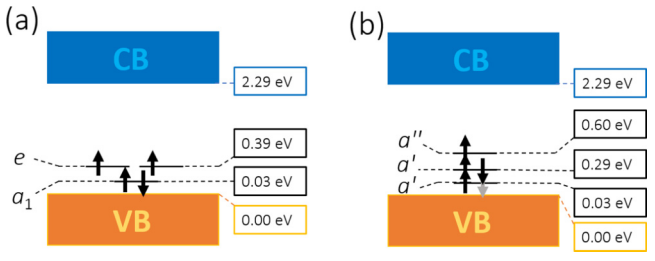

FIG. 3. Single particle spectrum of (a) ground and (b) excited states. Electron spins are represented by black arrows, the reminiscent hole after the optical excitation is depicted as a gray arrow.

We note that the simulation does not include the long wavelength phonons because of the finite size of the supercell, which requires an embedding method (e.g., Ref. 33); therefore, the S factor is a bit underestimated. The missing low wavelength phonons in the simulation lead to an artificial gap between the ZPL peak and the

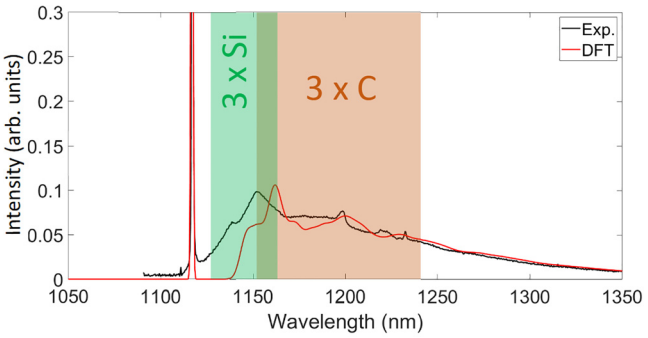

FIG. 4. Photoluminescence spectrum of divacancy in bulk 3C SiC. Black curve is an experimental spectrum (Exp.) recorded at near cryogenic temperature as reported in Ref. 16. Red curve (DFT) is the simulated HR emission spectrum at $T = 0$ K from DFT calculations. Energy of the phonon modes localized on the 3 $\times$ Si atoms around V_C falls in the $\approx$ 18–40 meV region (green shaded area), while that of the 3 $\times$ C atoms around V_{Si} falls into the $\approx$ 35–120 meV region (orange shaded area).

onset of phonon sideband (PSB). Furthermore, the relatively sharp peaks in PSB might be smoothened when the effect of the low wavelength phonons could be added to the simulation. This could affect the simulated PL spectrum too at elevated temperatures in terms of the appearance of the ZPL peak. We applied 3 meV gaussian broadening around all peaks in the phonon sideband to mitigate this problem. Despite the shortcomings of the finite supercell size mentioned above, the agreement between the experimental and the simulated PL spectra is very good, thus our approach is well established for analyzing the structure of PSB.

The PL spectrum of divacancy consists of a sharp ZPL with several longer wavelength (or smaller energy) peaks in the phonon sideband at T = 0 K temperature. The ZPL and the onset of PSB are separated by a ≈15 meV gap and the broadening of the PSB is about 250 meV (about 300 nm). As we noted above the separation between the ZPL peak and the onset of PSB is an artifact of the supercell size, which may also affect the position associated with the quasilocal phonon modes in the PL spectrum. We find a rich set of phonon-assisted optical transitions mainly related to the phonons localized on the 3 × C atoms around the V_{Si} and the 3 × Si atoms around the V_C (cf. Fig. 1). Our IPR analysis implies that in the phonon energy region of ≈18–40 meV (shift of 20–42 nm with respect to ZPL) the phonon modes mostly localized on the 3 × Si atoms with the IPR of ≈1–5, while phonon modes with energy falling in the ≈35–120 meV (shift of 36–133 nm with respect to ZPL) region are mainly localized on the 3 × C atoms with similar IPR in the simulated spectrum which appears at about 10 nm shorter wavelength in the experimental spectrum. The strongest feature in the simulated PSB appears between 1160 and 1170 meV (1060–1069 nm), i.e., in the intersection of the 3 × C and 3 × Si phonon mode region (cf. Fig. 4) demonstrating that phonon modes localized on both 3 × C and 3 × Si atoms contribute to this feature, resulting at least twice as large amplitude as any other peaks in the PSB.

The numerical temperature-dependent emission spectrum is shown in Fig. 5. The emission spectrum was calculated at the temperatures of $T = \{0, 150, 300, 450, 600\}$ K. Amplitudes of sharp features in the PSB decrease by elevating the temperature and at 450 K they become almost entirely smeared in our simulation.

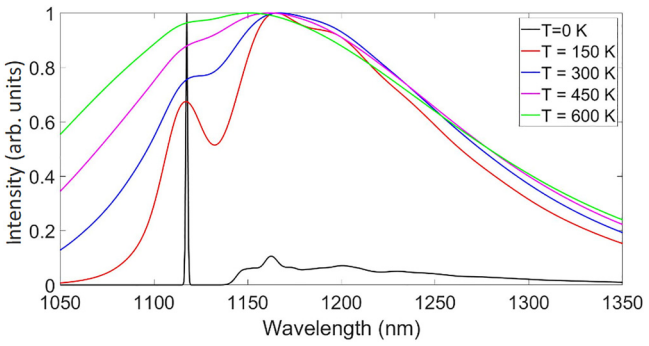

FIG. 5. Calculated temperature-dependent HR emission spectrum of divacancy in bulk 3C SiC at temperatures of 0 K (black line), 150 K (red line), 300 K (blue line), 450 K (magenta line), and 600 K (green line).

The missing long wavelength phonons in the simulation will not broaden the spectrum around the ZPL peak which is an artifact of the supercell size. In experiments, the ZPL peak becomes almost invisible due to the broadening of the long wavelengths phonon bands. Nevertheless, the overall temperature broadening of the PL spectrum, in particular, the long wavelength tail, should be well described by our simulations.

We further note that the absorption spectrum is basically the mirror image of the PL, reflected horizontally about the wavelength of the ZPL. This means that, by increasing the temperature, transition probability at lower than ZPL energies also increases providing the possibility of optical excitation at a longer wavelength than ZPL energies, i.e., anti-Stokes excitation, that has been observed for Si-vacancy in 4H SiC.[47]

C. Room-temperature PL emission spectrum in porous and nanocrystalline cubic SiC

As divacancy consists of nearby Si-vacancy and C-vacancy, the obvious method to form this defect is to irradiate SiC crystal for kicking out the Si and C atoms from their crystalline positions and then apply annealing to create them (e.g., Ref. 24). In this process, the irradiation species should have enough energy to kick out the heavy silicon atoms besides the light carbon atoms. By appropriate annealing temperature, the vacancies start to migrate and form complexes with each other where the simplest complex is the divacancy. However, not all the vacancies join in the process or they may form even larger complexes,[24] thus parasitic defects of vacancy clusters, interstitial clusters, and antisite complexes may coexist with divacancies by creating strain fields around the target divacancy defects. This will affect the PL spectrum, and if they are paramagnetic, then the spin properties of divacancies may be deteriorated. As a consequence, the PL spectrum for the ensemble of divacancies is an indicator about the possible overall performance of these divacancy qubits when referenced to the PL spectrum of divacancy in high quality cubic SiC or single defect measurements.

High quality formation of divacancies in SiC should attempt to avoid irradiation techniques. This scenario is not impossible by recognizing the fact that divacancies were observed in so-called high-purity semi-insulating (HPSI) 4H SiC (e.g., Ref. 15) which were grown by the hot wall CVD process far from the equilibrium process. On the other hand, high temperature growth of 3C SiC is not likely as high temperature prefers the formation of hexagonal SiC. However, our group has recently discovered that if Si-deficient 3C SiC is formed by adding aluminum or boron precursor in the growth process and surface carbon vacancy is introduced to the 3C SiC NPs by the etching process, then very low temperature annealing is able to transform these defects to divacancy complex because of the very short distance between the vacancies in few nanometer SiC NPs.[28] Thus, divacancies can be formed without the use of any strongly invasive irradiation techniques. On the other hand, the surface itself with 1–2 nm distance can also represent a strain field toward the divacancies that can influence its PL spectrum. Again, ensemble measurements on the PL spectrum of divacancies in this sample may reveal the quality of divacancy quantum bits.

To represent the two scenarios, we used two batches of samples. First, we created porous 3C SiC and irradiated with

neutrons (p-SiC). This porous SiC is built up from ca. 5 nm interconnected SiC NPs, very similar to the nanoparticles described later, but the material can be handled as bulk SiC. The advantage of neutron species compared to other ones like ions is that the whole porous sample is uniformly exposed to the irradiation to form vacancies. Second, we created divacancies in few nanometer 3C SiC NPs (SiC-NP) by means of chemistry. The details of the preparation of the two types of samples were given in the Methodology section. Finally, room temperature PL spectrum was recorded for both samples in our experiments because they should operate at room temperature as ODMR biomarkers.

The PL spectrum of porous 3C SiC is plotted in Fig. 6(a). We found background emission of other defects with a local maximum intensity at about 950 nm, which has some overlap with the PL signal of divacancies around the position of the ZPL peak (invisible in the experiment at room temperature). In our paper, we focus on the analysis of the divacancies' PL spectrum, which may have low overlap at the highest intensity in PSB. By comparing this spectrum with the reference PL spectrum in Fig. 4, a shift is visible in the emission spectrum. In order to quantify it, we took the simulation spectrum at room temperature (Fig. 5) and then shifted the entire spectrum in the energy region to closely reproduce the experimental spectrum taken from the porous SiC [see Fig. 6(b)]. We obtain +44 nm (−38.41 meV) redshift.

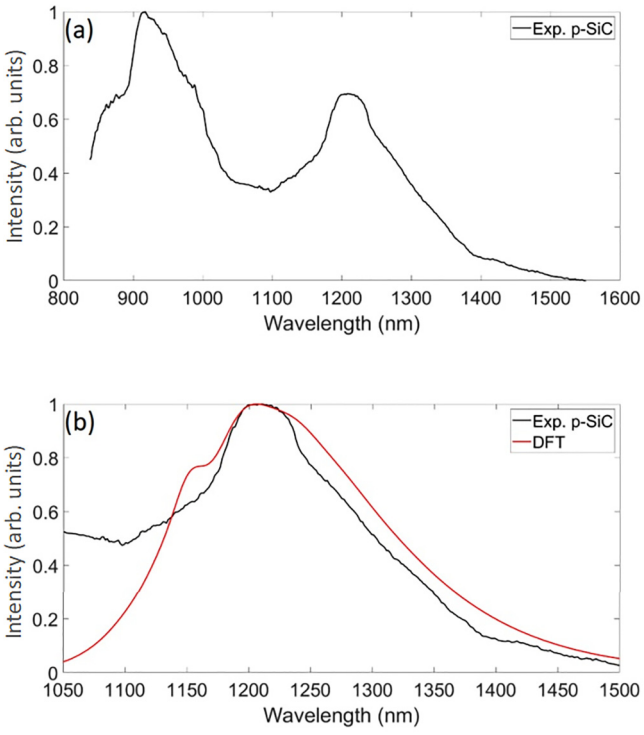

FIG. 6. (a) Room-temperature PL spectrum of the porous SiC (p-SiC) sample. Fluorescence at shorter wavelengths from residual defects is visible with a tail of the spectrum overlapping with the PL signal of divacancy. (b) Room-temperature PL spectra as obtained by DFT calculations (red curve) and experiments for the porous SiC sample (black curve). Both spectra are normalized for the sake of comparison.

The PL spectrum of 3C SiC NPs is plotted in Fig. 7. Here, we have no overlap from other defects as expected from the nature of the creation of the defect. We applied the same fitting procedure on the simulated PL spectrum as explained above for that of porous SiC. We obtain −8 nm (+7.30 meV) blueshift in this process.

Room temperature PL signals in the p-SiC samples as well as SiC-NP samples could be observed. We note that hexagonal inclusions or stacking faults in these materials may play a role in the room temperature stability of the divacancies' PL signals similar to the case of PL5 and PL6 centers in 4H SiC,[15] where stacking faults stabilize their room temperature magneto-optical signals.[48,49] We find that the shift parameter in the simulated room temperature PL spectrum of the SiC-NP samples is favorable over that of the p-SiC samples, and no residual fluorescence is observable. This implies that our chemistry process may produce higher quality divacancy quantum bits in ultrasmall 3C SiC NPs than those from traditional irradiation techniques.

IV. SUMMARY

We analyzed the PL spectrum of divacancies in 3C SiC. We find that the Debye–Waller factor is indeed favorable (about 7%) over that of other divacancy configurations in 4H SiC as the previous experimental data implied.[16] We identified the origin of the highest intensity in the phonon sideband which is an overlap of the motion of the nearest neighbor carbon and silicon atoms around the vacancies. Our analysis indicates that the ZPL linewidth broadens more at elevated temperatures than that of the NV center in diamond. By having relatively good accuracy in the simulated PL spectrum, we applied this to interpret the PL spectrum of divacancies recorded in neutron irradiated porous 3C SiC and in few nanometer diameter 3C SiC NPs. We find that the chemistry method produces less residual defects besides divacancies than irradiation techniques with annealing do, which implies that high quality divacancy quantum bits may be created by the chemistry method. Nevertheless, further studies are needed to strengthen this conclusion, and the spin properties should be explored in detail in few nanometer 3C SiC NPs.

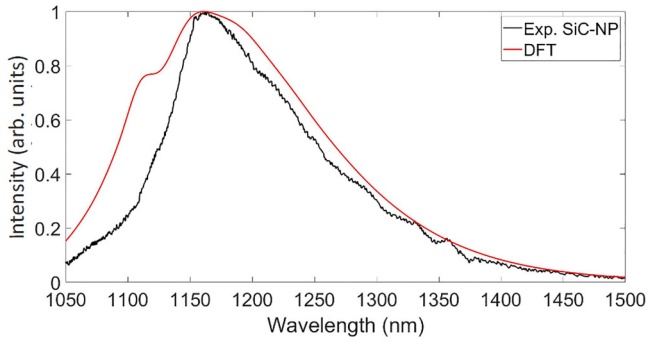

FIG. 7. Room-temperature PL spectra as obtained by DFT calculations (red curve) and experiments for the SiC-NP sample (black curve). Both spectra are normalized for the sake of comparison.

ACKNOWLEDGMENTS

A.G. acknowledges the National Research, Development, and Innovation Office of Hungary for Grant No. 127902 (QuantERA project Nanospin), the National Excellence Program for Grant No. KKP129866 (Quantum-coherent materials project), and the Quantum Information National Laboratory supported by the Ministry of Innovation and Technology of Hungary, as well as the EU Commission for the H2020 Quantum technology Flagship projects ASTERIQS (Grant No. 820394) and QuanTelCO (Grant No. 862721).

AUTHOR DECLARATIONS

Conflict of Interest

The authors declare no conflict of interest.

DATA AVAILABILITY

The data that support the findings of this study are available from the corresponding author upon reasonable request.

REFERENCES

[1]G. Zhang, Y. Cheng, J.-P. Chou, and A. Gali, Appl. Phys. Rev. **7**, 031308 (2020).
[2]G. Wolfowicz, F. J. Heremans, C. P. Anderson, S. Kanai, H. Seo, A. Gali, G. Galli, and D. D. Awschalom, Nat. Rev. Mater. **6**, 906 (2021).
[3]S. Castelletto, B. C. Johnson, V. Ivády, N. Stavrias, U. T. A. Gali, and T. Oshima, Nat. Mater. **13**, 151 (2014).
[4]A. Lohrmann, N. Iwamoto, Z. Bodrog, S. Castelletto, T. Ohshima, T. J. Karle, A. Gali, P. S. J. C. McCallum, and B. C. Johnson, Nat. Commun. **6**, 1009 (2015).
[5]M. Widmann, S.-Y. Lee, T. Rendler, N. T. Son, H. Fedder, S. Paik, L.-P. Yang, N. Zhao, S. Yang, I. Booker, A. Denisenko, M. Jamali, S. A. Momenzadeh, I. Gerhardt, T. Ohshima, A. Gali, E. Janzén, and J. Wrachtrup, Nat. Mater. **14**, 164 (2015).
[6]D. J. Christle, A. L. Falk, P. Andrich, P. V. Klimov, J. Ul Hassan, N. T. Son, E. Janzén, and T. Ohshima, and D. D. Awschalom, Nat. Mater. **14**, 160 (2015).
[7]M. Radulaski, M. Widmann, M. Niethammer, J. L. Zhang, S.-Y. Lee, T. Rendler, K. G. Lagoudakis, N. T. Son, E. Janzén, T. Ohshima, J. Wrachtrup, and J. Vučković, Nano Lett. **17**, 1782 (2017).
[8]S.-Y. Lee, M. Niethammer, and J. Wrachtrup, Phys. Rev. B **92**, 115201 (2015).
[9]H. Kraus, V. A. Soltamov, F. Fuchs, D. Simin, A. Sperlich, P. G. Baranov, G. V. Astakhov, and V. Dyakonov, Sci. Rep. **4**, 2012 (2015).
[10]D. Simin, V. A. Soltamov, A. V. Poshakinskiy, A. N. Anisimov, R. A. Babunts, D. O. Tolmachev, E. N. Mokhov, M. Trupke, S. A. Tarasenko, A. Sperlich, P. G. Baranov, V. Dyakonov, and G. V. Astakhov, Phys. Rev. X **6**, 031014 (2016).
[11]D. Simin, F. Fuchs, H. Kraus, A. Sperlich, P. G. Baranov, G. V. Astakhov, and V. Dyakonov, Phys. Rev. Appl. **4**, 014009 (2015).
[12]M. Niethammer, M. Widmann, S.-Y. Lee, P. Stenberg, O. Kordina, T. Ohshima, N. T. Son, E. Janzén, and J. Wrachtrup, Phys. Rev. Appl. **6**, 034001 (2016).
[13]C. J. Cochrane, J. Blacksberg, M. A. Anders, and P. M. Lenahan, Sci. Rep. **6**, 1239 (2016).
[14]A. N. Anisimov, D. Simin, V. A. Soltamov, S. P. Lebedev, P. G. Baranov, G. V. Astakhov, and V. Dyakonov, Sci. Rep. **6**, 5067 (2016).
[15]W. F. Koehl, B. B. Buckley, F. J. Heremans, G. Calusine, and D. D. Awschalom, Nature **479**, 84 (2011).
[16]D. J. Christle, P. V. Klimov, C. F. de las Casas, K. Szász, V. Ivády, V. Jokubavicius, J. Ul Hassan, M. Syväjärvi, W. F. Koehl, T. Ohshima, N. T. Son, E. Janzén, A. Gali, and D. D. Awschalom, Phys. Rev. X **7**, 021046 (2017).
[17]P. G. Baranov, I. V. Il'in, E. N. Mokhov, M. V. Muzafarova, S. B. Orlinskii, and J. Schmidt, JETP Lett. **82**, 441 (2005).
[18]N. T. Son, P. Carlsson, J. ul Hassan, E. Janzén, T. Umeda, J. Isoya, A. Gali, M. Bockstedte, N. Morishita, T. Ohshima, and H. Itoh, Phys. Rev. Lett. **96**, 055501 (2006).
[19]V. Y. Bratus, R. S. Melnik, S. M. Okulov, V. N. Rodionov, B. D. Shanina, and M. I. Smoliy, Phys. B **404**, 4739 (2009).
[20]A. Gali, A. Gällström, N. T. Son, and E. Janzén, Mater. Sci. Forum **645-648**, 395 (2010).
[21]A. Gali, Phys. Status Solidi B **248**, 1337 (2011).
[22]N. T. Son, E. Sörman, W. M. Chen, C. Hallin, O. Kordina, B. Monemar, E. Janzén, and J. L. Lindström, Phys. Rev. B **55**, 2863 (1997).
[23]E. Janzén, A. Henry, J. P. Bergman, A. Ellison, and B. Magnusson, Mater. Sci. Semicond. Process **4**, 181 (2001).
[24]W. E. Carlos, N. Y. Garces, E. R. Glaser, and M. A. Fanton, Phys. Rev. B **74**, 235201 (2006).
[25]A. M. Smith, M. C. Mancini, and S. Nie, Nat. Nanotechnol. **4**, 710 (2009).
[26]B. Somogyi, V. Zólyomi, and A. Gali, Nanoscale **4**, 7720 (2012).
[27]B. Somogyi and A. Gali, J. Phys.: Condens. Matter **26**, 143202 (2014).
[28]D. Beke, J. Valenta, G. Károlyházy, S. Lenk, Z. Czigány, B. G. Márkus, K. Kamarás, F. Simon, and A. Gali, J. Phys. Chem. Lett. **11**, 1675 (2020).
[29]A. L. Falk, B. B. Buckley, G. Calusine, W. F. Koehl, V. V. Dobrovitski, A. Politi, C. A. Zorman, P. X.-L. Feng, and D. D. Awschalom, Nat. Commun. **4**, 076401 (2013).
[30]D. Beke, G. Károlyházy, Z. Czigány, G. Bortel, K. Kamarás, and A. Gali, Sci. Rep. **7**, 645 (2017).
[31]K. Huang, A. Rhys, and N. F. Mott, Proc. R. Soc. London, Ser. A **204**, 406 (1950).
[32]A. Gali, D. T. M. Vörös, G. Thiering, E. Cannuccia, and A. Marini, Nat. Commun. **7**, 1012 (2016).
[33]A. Alkauskas, B. B. Buckley, D. D. Awschalom, and C. G. V. de Walle, New J. Phys. **16**, 073026 (2014).
[34]A. Csóré, I. G. Ivanov, N. T. Son, and A. Gali, "Photoluminescence lineshapes and charge state control of divacancy qubits in silicon carbide," arXiv:2107.01971 [cond-mat.mes-hall] (2021).
[35]P. Debye, Ann. Phys. **348**, 49 (1913).
[36]I. Waller, Z. Phys. **17**, 398 (1923).
[37]K.-M. C. Fu, C. Santori, P. E. Barclay, L. J. Rogers, N. B. Manson, and R. G. Beausoleil, Phys. Rev. Lett. **103**, 256404 (2009).
[38]J. Heyd, G. E. Scuseria, and M. Ernzerhof, J. Chem. Phys. **118**, 8207 (2003).
[39]A. Gali, E. Janzén, P. Deák, G. Kresse, and E. Kaxiras, Phys. Rev. Lett. **103**, 186404 (2009).
[40]P. E. Blöchl, Phys. Rev. B **50**, 17953 (1994).
[41]G. Kresse and J. Furthmüller, Phys. Rev. B **54**, 11169 (1996).
[42]I. B. Bersuker, *The Jahn-Teller Effect* (Cambridge University Press, 2006).
[43]J. P. Perdew, K. Burke, and M. Ernzerhof, Phys. Rev. Lett. **77**, 3865 (1996).
[44]R. J. Bell, P. Dean, and D. C. Hibbins-Butler, J. Phys. C: Solid State Phys. **3**, 2111 (1970).
[45]G. Thiering and A. Gali, Phys. Rev. B **96**, 081115 (2017).
[46]B. Magnusson, N. T. Son, A. Csóré, A. Gällström, T. Ohshima, A. Gali, and I. G. Ivanov, Phys. Rev. B **98**, 195202 (2018).
[47]J.-F. Wang, F.-F. Yan, Q. Li, Z.-H. Liu, J.-M. Cui, Z.-D. Liu, A. Gali, J.-S. Xu, C.-F. Li, and G.-C. Guo, Nat. Commun. **12**, 682 (2021).
[48]V. Ivády, J. Davidsson, N. Delegan, A. L. Falk, P. V. Klimov, S. J. Whiteley, S. O. Hruszkewycz, M. V. Holt, F. J. Heremans, N. T. Son, D. D. Awschalom, I. A. Abrikosov, and A. Gali, Nat. Commun. **10**(1), S807 (2019).
[49]Q. Li, J.-F. Wang, F.-F. Yan, J.-Y. Zhou, H.-F. Wang, H. Liu, L.-P. Guo, X. Zhou, A. Gali, Z.-H. Liu, Z.-Q. Wang, K. Sun, G.-P. Guo, J.-S. Tang, H. Li, L.-X. You, J.-S. Xu, C.-F. Li, and G.-C. Guo, "Room temperature coherent manipulation of single-spin qubits in silicon carbide with a high readout contrast," Natl. Sci. Rev. (published online, 2021).